# Template-Induced Structuring and Tunable Polymorphism of Three-Dimensionally Ordered Mesoporous (3DOm) Metal Oxides

Daniel G. Gregory,[†,§] Qianying Guo,[†,§] Li Lu,[‡] Christopher J. Kiely,[†,‡] and Mark A. Snyder*,[†]

[†]Department of Chemical and Biomolecular Engineering and [‡]Department of Materials Science and Engineering, Lehigh University, Bethlehem, Pennsylvania 18015, United States

ABSTRACT: Convectively assembled colloidal crystal templates, composed of size-tunable (ca. 15−50 nm) silica (SiO_2) nanoparticles, enable versatile sacrificial templating of three-dimensionally ordered mesoporous (3DOm) metal oxides (MO_x) at both mesoscopic and microscopic size scales. Specifically, we show for titania (TiO_2) and zirconia (ZrO_2) how this approach not only enables the engineering of the mesopore size, pore volume, and surface area but can also be leveraged to tune the crystallite polymorphism of the resulting 3DOm metal oxides. Template-mediated volumetric (i.e., interstitial) effects and interfacial factors are shown to preserve the metastable crystalline polymorphs of each corresponding 3DOm oxide (i.e., anatase TiO_2 (A-TiO_2) and tetragonal ZrO_2 (t-ZrO_2)) during high-temperature calcination. Mechanistic investigations suggest that this polymorph stabilization is derived from the combined effects of the template−replica (MO_x/ SiO_2) interface and simultaneous interstitial confinement that limit the degree of coarsening during high-temperature calcination of the template−replica composite. The result is the identification of a facile yet versatile templating strategy for realizing 3DOm oxides with (i) surface areas that are more than an order of magnitude larger than untemplated control samples, (ii) pore diameters and volumes that can be tuned across a continuum of size scales, and (iii) selectable polymorphism.
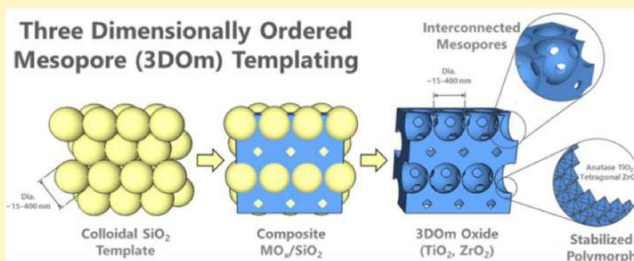
INTRODUCTION

Significant attention has been focused on the development of ordered mesoporous transition-metal oxides because of their intrinsic catalytic character and thermodynamic stability at elevated temperatures[1−3] and thus their attractiveness for current and emerging applications spanning adsorption, catalysis, solar cells, and energy storage, among others.[4] Commercial metal oxide powders are often manufactured industrially via high-temperature flame hydrolysis techniques, which results in the formation of agglomerations of primary crystallites.[5] These aggregated powders commonly form a random, tortuous network of interconnected pores with moderate surface areas and broad distributions in pore size.[6] The inherent irregularity of the pore structure can lead to molecular transport limitations that, for example, hinder the performance of an adsorbent, result in excessive catalyst coking, or generate hot spots within a reactor.[7−9] These problems are compounded by the susceptibility of oxides to thermodynamic mechanisms of reconfiguration including sintering, coarsening, and polymorph transformation when employed in high-temperature applications.[10] Thus, the identification of versatile strategies capable of tailoring properties ranging from porosity to polymorphism across a diverse materials palette is essential to the rational engineering of existing metal oxides and the development of new nanomaterials for specific applications.

The development of sacrificial, template-directed synthesis methods has been widely explored as a means of constructing porous oxides with tailored porosities within the mesoporous regime (i.e., 2−50 nm)[11] from materials characterized, in their native state, by lower surface areas, restrictive pore volumes, and/or fine powder morphologies. Templating strategies are generally categorized by the nature of the template as either hard (i.e., preformed organic or inorganic structures such as colloids,[12−14] colloidal crystals,[15,16] and ordered porous solids[17,18]) or soft (i.e., molecular or macromolecular structures[19]). Soft templating benefits from its one-pot approach but relies on solution thermodynamics for the simultaneous assembly of sacrificial porogens with molecular replica precursors. Fine control over mesopore size and topology is possible, owing, for example, to strategies for controlling micelle size and the liquid-crystalline assembly of porogen networks. However, control over the pore wall thickness is more challenging, and porogen−replica interactions tend to complicate efforts for the a priori, rational engineering of materials with specific properties. Moreover, the temperature sensitivity of the soft templates leads to amorphous or only partially crystallized mesoporous MO_x and pore shrinkage or even collapse upon thermal treatment owing to MO_x coarsening occurring simultaneously with the loss of the[1,20] organic template.

.

Hard templating, on the other hand, relies on the preformation of porous solids that are subsequently employed to cast a replica material phase. These approaches benefit from the decoupling of the template and replica formation processes, thereby expanding the accessible range of porous replica materials.[21−23] Drawbacks of conventional hard templating, however, stem from the common need to first form a template with tailored structural dimensions, a process often relying on soft-templating approaches (e.g., ordered mesoporous silicas (OMSs) among the SBA, MCM, and KIT families). While commonly employed for "hard"-templating or nanocasting of porous replica materials, the limited tunability of the pore walls within such OMSs translates to restrictions on the achievable pore sizes within replica mesoporous structures. In addition, successful replication can be challenged by the rapid hydrolysis and condensation of conventional oxide precursors,[24,25] which leads to precursor aggregation and prevents infiltration of the template materials. Templating is further complicated by the large volumetric change that occurs during syneresis and crystallization of the precursor.[26] Despite these challenges, numerous examples of successful nanocasting of ordered mesoporous oxides utilizing ordered mesoporous silicas

(particularly with KIT-6 and SBA-15) have been re-ported.[1,27−29]

Alternative modes of hard-templating have relied on colloidal crystals as templates, the benefits of which relate to their intrinsic interstitial rather than templated porosity, the three-dimensional interconnectivity of the particle network, and the coupled tunability of the constituent particle and interstice size.[12,15,20,22,30 ,31] These properties translate, respectively, to facile template formation, ease of replica precursor infiltration, and the formation of porous replicas composed of three-dimensionally ordered and interconnected spherical pore bodies with pore walls of tunable thickness. The most common colloidal crystal templating of porous MO_x materials has exploited crystals composed of monodisperse micrometer or submicrometer constituent particles, leading to the templating of lower-surface-area three-dimensionally ordered macroporous (3DOM)[1,12 ,15,20,22] rather than mesoporous (3DOm) struc-tures. Only recently have methods for the facile synthesis of silica nanoparticle crystals composed of constituent SiO_2 nanoparticles[21,32,33] been identified and leveraged for the synthesis of 3DOm MO_x materials.[30] In those cases, the near-nanometer resolution with which the constituent nano-particles can be tuned between ca. 10−50 nm helps to bridge the macropore−mesopore gap that has persisted until recently with hard-templated porous materials.[15]

The growth of synthetic strategies for tailoring nanoparticle shape, size, and multimodal assembly[34−36] highlights the potential for nanoparticle crystal templating of hierarchically complex replica MO_x materials with tailored pore size, connectivity, and topology. Such topological control holds promise for modulating properties such as internal molecular transport.

In addition, the ability to choose the polymorphic state of a given transition-metal oxide can be critical for realizing specific functions. For example, recent photocatalytic studies involving porous TiO_2 have revealed the importance of having mixtures of anatase and rutile polymorphs for optimal electron hole−pair separation.[37−42] Additionally, specific polymorphism (i.e., exclusively having anatase or rutile) has been shown to be critical to the development of active catalytic supports.[39,41,43] Similarly, transformation from the metastable tetragonal ZrO_2

polymorph to the more-stable monoclinic polymorph has been shown to coincide with the evolution of surface functionality in ZrO_2-based acid catalysts; this can be utilized to tailor the surface chemistry and optimize the catalytic performance.[44,45] Calcination can be used to induce polymorph interconversion and enhance crystallinity; however, it is generally a poor means of fine tuning the proportions of phases present in fractional polymorphism and is often accompanied by unwanted sintering and coarsening. As such, there is a clear need to identify an independent means of tuning the polymorphic character of highly crystalline metal oxides while preserving porosity and surface area at elevated temperatures.

In this work, we demonstrate the formation of pore-size-tunable, three-dimensionally ordered mesoporous (3DOm) TiO_2 and ZrO_2 materials using colloidal crystal templates composed of monodisperse, size-tunable (ca. 10−50 nm) SiO_2 nanoparticles. By synthesizing particles of representative sizes spanning this once-elusive particle size range, we show how the ability to tailor the constituent template particle size with nanometer resolution and the limited shrinkage of the replica pores translate to high-surface-area, three-dimensionally ordered mesoporous (3DOm) MO_x with directly tunable pore sizes. Additionally, we identify a synergistic, template-mediated interfacial and volumetric mechanism for stabilizing metastable metal oxide polymorphs and fine-tuning fractional polymorphism upon high-temperature processing. We demon-strate this effect for TiO_2 (i.e., anatase TiO_2) and employ ZrO_2 (i.e., tetragonal ZrO_2) as a surrogate metal oxide for establishing the generalizability of 3DOm templating for tailoring both the mesostructure (i.e., pore size and surface area) and the crystallography (i.e., polymorphism) of porous oxides.

■ EXPERIMENTAL SECTION

Synthesis of Colloidal Crystal Templates. Colloidal crystal templates consisting of monodisperse, spherical SiO_2 nanoparticles (SiO_2-NPs; diameter ~15−50 nm) were prepared via an amino acid-mediated synthesis and convective assembly process as reported previously by us[21,31 ,32] and others. [33,46] Generally, SiO_2-NP sols were synthesized by the hydrolysis of tetraethylorthosilicate (TEOS) in aqueous solutions of L-lysine (L-lysine ≥98%, Sigma-Aldrich) at 90 °C under vigorous stirring. Nanoparticles of ca. 15 nm ($x = 120$, $y = 2.46$) and 22 nm ($x = 61.5$, $y = 1.23$) nominal diameter were synthesized from solutions with final molar compositions after hydrolysis of x SiO_2/y L-lysine/9500 H_2O/4x ethanol. Sols of larger ca. 28 nm ($x = 420$, $y = 2.46$), ca. 34 nm ($x = 690$, $y = 1.23$), and 50 nm ($x = 1120$, $y = 1.23$) particles were prepared through a seeded growth process involving 1−3 sequential TEOS additions to the ca. 15 nm seed particle solutions until the prescribed molar composition was reached, with intermediate stirring for 12−24 h at 90 °C.[21] The prepared silica sols were filtered (0.2 μm disc filter), dried into colloidal crystals at 70 °C, and in some cases calcined to 600 °C (5 h soak). Larger ca. 400 nm SiO_2 particles were synthesized by a modified arginine-mediated process,[33,47] wherein TEOS was first hydrolyzed in an aqueous solution of the amino acid arginine under vigorous stirring for 10 min at room temperature, followed by heating at 70 °C for 24 h leading to

a final molar composition of 17.9 SiO_2/0.10 arginine/1000 H_2O/71.8 ethanol. A 0.02 mL aliquot of this sol was then used to seed the growth of 400 nm SiO_2 particles by mixing with 175.3 g of a solution of molar composition 0.65 arginine/1000 H_2O/1261.9 ethanol for the subsequent hydrolysis of 10.4 g of TEOS under vigorous stirring at 70 °C.

Synthesis of Three-Dimensionally Ordered Mesoporous (3DOm) and Untemplated TiO_2 or ZrO_2. Three-dimensionally ordered mesoporous (3DOm) TiO_2 and ZrO_2 materials were prepared via iterative incipient wetness infiltration (IWI) of preformed SiO_2

colloidal crystal templates (SiO$_2$-NP templates) with oxide precursor solutions. TiO$_2$ precursor solutions were prepared according to ref 29 by precipitating titanium(IV) ethoxide (Ti(OC$_2$H$_5$)$_4$, Aldrich) in deionized (DI) water under vigorous stirring (e.g., 0.6 g Ti(OEt)$_4$, 30 mL water) for 1 h prior to centrifugation and solvent decantation. The resulting titanium hydroxide gel was redispersed in concentrated hydrochloric acid (e.g., 0.8 g HCl per batch), yielding a clear solution. Clear aqueous ZrO$_2$ precursor solutions were prepared from zirconyl chloride octahydrate (ZrOCl$_2$·8H$_2$O, Sigma-Aldrich) in DI water (1.0 M ZrOCl$_2$·8H$_2$O). Aliquots of these clear precursor solutions (~0.5−1.0 mL/(g SiO$_2$-NP templates)) were deposited within the SiO$_2$-NP templates via an iterative IWI procedure with intermediate drying for 10 min at either 120 °C (ZrO$_2$) or 160 °C (TiO$_2$) and final drying at 100 °C for 24 h. In the case of 3DOm TiO$_2$, iterative IWI was carried out nine times; similarly, the IWI process was repeated until enough Zr material was added to fill either 20% (ZrO$_2$ ≈ 18 wt %) or 100% (ZrO$_2$ ≈ 53 wt %) of the template void space with crystalline ZrO$_2$. The composite TiO$_2$/SiO$_2$-NP powders were calcined at 1 °C/min to 450 or 773 °C (5 h dwell); similarly, the composite ZrO$_2$/SiO$_2$-NP powders were calcined at 5 °C/min to a final temperature ranging from 500 to 1000 °C (3 h dwell). Selective etching of the silica templates was carried out in a 1.0 M aqueous sodium hydroxide solution (NaOH, EMD) at room temperature for 5 days, with daily replacement of the NaOH solution. Processing conditions for the templated samples are denoted herein by x-T$_c$-SD-T$_s$, with the x prefix denoting the oxide (i.e., x = T for TiO$_2$, x = Z for ZrO$_2$), followed by the calcination temperature (T$_c$) of the composite MO$_x$/SiO$_2$-NP powder, the diameter of the SiO$_2$ nanoparticles (SD), and finally the calcination temperature of the template (T$_s$).

Untemplated MO$_x$ control powders were prepared in the absence of the silica template by drying of the clear MO$_x$ precursor solution in a ceramic boat per the sequential conditions described above for TiO$_2$ and directly at room temperature (72 h) in the case of ZrO$_2$. The resulting powders were ground with a mortar and pestle, sieved with a #40 mesh screen (0.420 mm pores), and calcined to a temperature of T$_c$, according to the aforementioned conditions. These untemplated, u, TiO$_2$ and ZrO$_2$ samples are referenced herein as x-u-T$_c$, where x again denotes the specific oxide (i.e., T for TiO$_2$, Z for ZrO$_2$). Physical mixtures (ca. 50 wt %) of SiO$_2$ (35−50 nm) with TiO$_2$ and ZrO$_2$ were also prepared by grinding the SiO$_2$-NP templates with respective untemplated TiO$_2$ and ZrO$_2$ powders, the latter prior to their calcination, for 15 min using a mortar and pestle. The composite powders were sieved with a #40 mesh screen and calcined.

Characterization of the TiO$_2$ and ZrO$_2$ Products. Physical characteristics of the colloidal crystal templates and 3DOm oxides were measured via nitrogen physisorption (77 K) using a Micromeritics ASAP 2020 instrument following degassing at 200 °C for 48 h (5 °C/min ramp). The specific surface area and the pore size distribution were calculated using the Brunauer−Emmett−Teller (BET) and Barrett−Joyner−Halenda (BJH) methods, respectively,[48,49] applied to the adsorption branch. The micropore volume and external surface area were analyzed by conventional t-plot methods, and the total pore volume was calculated from the volume adsorbed at P/P$_0$ ≈ 0.99.

TEM imaging of powdered samples dispersed on an ultrathin carbon film supported on a 300-mesh copper grid (Electron Microscopy Sciences) was carried out on a LaB$_6$ JEOL JEM-2000FX instrument operating at 200 kV. Scanning transmission electron microscopy (STEM) was carried out on an aberration-corrected JEOL JEM-ARM200CF instrument operating at 200 kV.

TiO$_2$ and ZrO$_2$ crystallinity was analyzed via powder X-ray diffraction (XRD) using a Rigaku MiniFlex II diffractometer with Cu Kα radiation (λ$_{Kα}$ = 1.5418 Å). The polymorph volume percentage of anatase (A) relative to rutile (R) for TiO$_2$ samples and tetragonal (t) relative to monoclinic (m) for ZrO$_2$ samples was calculated from integrated Bragg reflection peaks, I$_i$, corresponding to polymorph i (i = A, R, m, t). Specifically, in the case of TiO$_2$ the anatase (A) volume percentage was calculated to be 100 × [I$_A$/(I$_R$ + 0.79I$_A$)], where I$_R$ is the integrated R(110) reflection at 2θ ≈ 27.5° and I$_A$ is the A(101) reflection at 2θ ≈ 25.3°.[51] For ZrO$_2$, the volume percentage of the

tetragonal (t) ZrO$_2$ polymorph was calculated to be 1 − [1.311X$_m$/(1 + 0.311X$_m$)], where X$_m$ is a weighted average of integrated peak intensities of the characteristic tetragonal (i.e., t(101) at 2θ ≈ 30.2°) and monoclinic (i.e., m(111) at 2θ ≈ 31.5° and m($\bar{1}$11) at 2θ ≈ 28.2°) reflections given by X$_m$ = [I$_m$($\bar{1}$11) + I$_m$(111)]/[I$_m\bar{1}$11) + I$_m$(111) + I$_t$(101)].[50] Scherrer analysis was carried out on powder XRD data to assess the mean crystallite size, τ, given as τ = kλ/(β cos θ), where k is the shape factor, λ is the wavelength, β is the line broadening at the full width at half-maximum intensity, and θ is the Bragg angle.[52]

Fourier transform infrared spectroscopy (FTIR) was conducted under ambient conditions using a Thermo Scientific Nicolet 10 instrument equipped with an attenuated total reflectance (ATR) attachment. The SiO$_2$ nanoparticles were dried at either 70 °C or calcined for 5 h at 600 °C and then quickly sealed in a glass vial to limit the physisorption of atmospheric moisture prior to FTIR analysis. After cooling to room temperature, the samples were removed from the vial and analyzed with FTIR spectroscopy.

■ RESULTS AND DISCUSSION

Template-Free Synthesis of Tunable Colloidal SiO$_2$ Templates. We and others have previously shown that aqueous amino acid (L-lysine)-mediated synthesis of SiO$_2$ nanoparticles (SiO$_2$-NPs) yields highly monodisperse particles with nearly continuously tunable diameters in the 10−50 nm range.[21,31–33,46] The evaporation-induced convective assembly of these particles[21,35] leads to the direct template-free formation of three-dimensionally ordered mesoporous silica structures shown via TEM imaging in Figure S1 and referred to hereafter according to the nominal size of the constituent SiO$_2$-NPs (e.g., 34 nm SiO$_2$-NP structures). Nitrogen physisorption isotherms collected on nominal 15, 22, 28, and 34 nm SiO$_2$-NP structures are type IV (Figure S2).[53] The type-H2 hysteresis that shifts to higher relative pressures with increasing SiO$_2$-NP size indicates a characteristic increase in the dimensions of mesopores, namely, the interstitial space within the SiO$_2$-NP assemblies, with increasing SiO$_2$-NP size.

Here, we have synthesized particles of representative sizes spanning the range accessible by the lysine-mediated synthesis process to demonstrate the ease and resolution with which particle size control and ultimate pore templating can be achieved with this approach. Namely, the coupled tunability of particle size and mesopore (i.e., interstitial) size (D$_{SiO_2}$ versus D$_{pore}$, Table S1) translates to the possibility for respective control over pore size and wall thickness in three-dimensionally ordered mesoporous (3DOm) materials formed through sacrificial replication (i.e., nanocasting) of the colloidal crystals. Here, using TiO$_2$ as a surrogate MO$_x$, we demonstrate how these SiO$_2$-NP structures can be employed as sacrificial hard templates of mesopore topology. We also investigate the expanded role of the template in impacting the polymorphism of the crystalline 3DOm replicas and finally explore the generalizability of this multiscale templating through extension to 3DOm ZrO$_2$ materials.

Hard Templating via IWI for the Synthesis of 3DOm TiO$_2$. Hard-templating requires the identification of suitable MO$_x$ precursors for complete volumetric infiltration of the interstitial pores of the sacrificial template. In cases such as the SiO$_2$-NP templates discussed here, where the template is composed of mesopores (ca. 4.4−13.9 nm, Table S1) rather than macropores, solutions of molecular or oligomeric precursors are required for high-fidelity template replication. We employed acid-mediated TiO$_2$ dissolution[29] as a means for realizing clear solutions containing monomeric and oligomeric TiO$_2$ precursors. Sequential incipient wetness infiltration (IWI)

of the colloidal crystal templates by aliquots of the clear solution enabled filling of the interstices of the SiO_2-NP templates. Subsequent drying, template-replica composite calcination at 450 °C, and selective template dissolution resulted in robust 3DOm TiO_2 materials. We refer hereafter to 3DOm structures according to the template particle size from which they were derived (e.g., 34 nm 3DOm TiO_2). Representative TEM micrographs of the 3DOm TiO_2 products shown in Figure 1a−d reveal the presence of ordered and 3D-
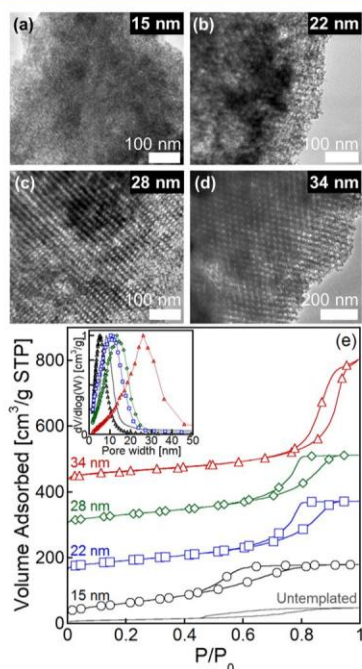

Figure 1. Representative TEM micrographs of 3DOm TiO_2 prepared by replication of silica nanoparticle crystal templates composed of nominal (a) 15, (b) 22, (c) 28, and (d) 34 nm silica nanoparticles. The composite TiO_2-SiO_2 samples were calcined at 450 °C to induce TiO_2 crystallization prior to removal of the colloidal crystal template. (e) Corresponding nitrogen physisorption isotherms and the associated pore size distributions (inset) resulting from BJH adsorption branch analysis that serve to demonstrate the tunability of the 3DOm TiO_2 mesopore size relative to untemplated TiO_2 materials. Isotherms in (e) have been shifted vertically for clarity.

interconnected spherical pore bodies of tailored dimension that are interconnected with hexagonally close-packed (hcp) symmetry by narrow windows at points of original contact between adjacent template particles. Representative SEM micrographs are shown for the 34 nm 3DOm TiO_2 in Figure S3. This ordered pore topology is in stark contrast to disordered intercrystalline pores within untemplated TiO_2 materials (Figure S4).

Nitrogen physisorption isotherms (Figure 1e) collected on the 3DOm samples are type IV and reveal a characteristic H2 hysteresis indicative of mesoporosity.[53] BJH analysis of the adsorption branch of the resulting isotherms confirms that the pore body size (D_{pore}, Table S2) and its distribution (inset, Figure 1e) trend proportionally to but are systematically lower than the constituent particle size of the SiO_2-NP templates. Comparative measurement of the center-to-center distances of ca. 100 template particles of 34 nm nominal diameter (Figure S 1d) with the center-to-center distance of pores within the 3DOm replica structure (Figure 1d) suggests only modest (ca.

2%) contraction of the 3DOm replica pores. Thus, the apparent discrepancy between the mesopore dimensions extracted via BJH analysis of the adsorption isotherms and the nominal template particle size appears to be primarily an artifact of the assumption of cylindrical rather than spherical pores that is intrinsic to the BJH method.[49]

In all cases, as shown in Table S2, sacrificial templating offers a dramatic increase in the BET surface area and total pore volume relative to those of untemplated control samples calcined under the same conditions. Specifically, for 3DOm TiO_2 samples calcined at 450 °C prior to template removal, specific surface areas span from 155 to 229 m^2/g over the range of template sizes explored (i.e., 34 to 15 nm, respectively). This marks a respective 288 to 473% increase in surface area relative to the corresponding untemplated TiO_2. Similarly, total specific pore volumes spanning 0.3 to 0.6 cm^3/g, associated nearly exclusively with mesopores, are derived from SiO_2-NP templating, whereas typical pore volumes of untemplated TiO_2 were measured at 0.1 cm^3/g. This analysis shows that the resulting 3DOm structures are predominantly mesoporous, with the statistical equivalence of the total and mesopore volumes. No more than ca. 6.5% of the overall surface area is associated with microporosity, most probably derived from intercrystalline pores within the nanoparticulate walls of the resulting structures.

Even with a further increase in the calcination temperature to 773 °C, which is more than 100 °C above the characteristic Hüttig temperature for bulk crystalline TiO_2 ($TiO_2^{Hüttig} \approx 610$ °C) where the onset of atomic surface mobility is expected to feed particle coarsening, consistently large specific surface areas (ca. 175 m^2/g) and pore volumes (0.4 cm^3/g) were retained. These data underscore the resistance that hard SiO_2-NP templates offer against pore collapse during the structural coarsening that is known to occur at high temperatures for crystalline MO_x materials. Hence, the facile ability to synthesize SiO_2-NP templates with tunable particle size can be leveraged as a versatile strategy for synthesizing ordered, porous TiO_2 structures with fine control over mesopore size as well as the realization of large mesopore volumes and high surface areas relative to those of untemplated materials.

Template-Induced Anatase Phase Stabilization in TiO_2. Powder X-ray diffraction (XRD) patterns shown in Figure 2 confirm the crystallization of 3DOm TiO_2 structures replicated on SiO_2-NP templates of various specified sizes following calcination of the template−replica composite to temperatures below (450 °C, Figure 2a) and above (773 °C, Figure 2b) the characteristic Hüttig temperature for bulk crystalline TiO_2. Traditionally, TiO_2 starts its polymorphic transformation from the metastable anatase (A(101) at $2\theta \approx$ 25.3°) to the thermodynamically stable rutile (R(110) at $2\theta \approx$ 27.5°) polymorph upon high-temperature calcination (i.e., ~500 °C), and the transformation is usually complete once the Hüttig temperature is reached.[54] This expected behavior for the polymorphic transformation is clearly demonstrated by the untemplated TiO_2 samples in our study, which are predominantly composed of the anatase polymorph (i.e., ~75% as tabulated in Table S2) when calcined at 450 °C (Figure 2a), whereas calcination at 773 °C induces complete transformation to the rutile polymorph (Figure 2b).

In stark contrast to this, the templated 3DOm TiO_2 samples all demonstrate a comparative preservation of the metastable anatase polymorph as noted by the general persistence of the A(101) reflection and limited development of the R(110)
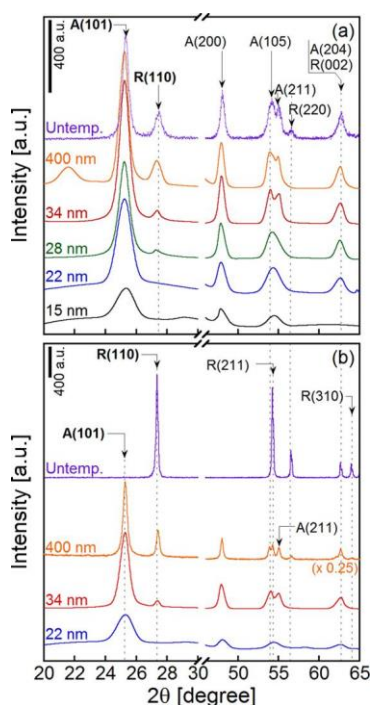
Figure 2. Comparison of XRD diffractograms of untempated TiO$_2$ control samples relative to 3DOm TiO$_2$ materials templated by 9× incipient wetness infiltrations (IWIs) of silica nanoparticle crystals with specified constituent particle sizes ranging from 15 to 400 nm and composite calcination at (a) 450 °C and (b) 773 °C. XRD diffractograms were collected after the selective etching of the SiO$_2$-NP templates.

reflection under both of the calcination conditions studied here. Specifically, for calcination at 450 °C (Figure 2a), the anatase fraction estimated for 15 to 34 nm 3DOm TiO$_2$ materials (Table S2) is no less than ca. 92%. Similarly, calcination at 773 °C (Figure 2b) leads to a 3DOm TiO$_2$ anatase volume fraction of no less than ca. 96%.

Powder XRD in Figure 2 and the fractional polymorphism estimated by Scherrer analysis and tabulated in Table S2 also reveal an apparent sensitivity of this polymorph stabilization to the template particle size. Specifically, the anatase volume fraction in 3DOm TiO$_2$ systematically decreases by up to 8% upon increasing the SiO$_2$-NP template size from 15 to 34 nm. As shown in Table S1, such changes in the template particle size correspond to an increase in template pore size (4.4−13.9 nm) and a decrease in template surface area (246−103 m^2/g). It is therefore conceivable that the observed polymorph stabilization may be derived, at least in part, from respective volumetric and interfacial factors imposed by the template during the formation of 3DOm replica structures.

Volumetric Contributions to the Stabilization of Metastable 3DOm Polymorphism. Free-energy-based argu-ments suggest that a critical nucleus size of ca. 15 nm[55,56] exists for TiO$_2$ below which the anatase polymorph is more stable than the rutile polymorph. The commensurate size of the SiO$_2$-NP template pores (ca. 4−14 nm, Table S1) wherein TiO$_2$ crystallization occurs during 3DOm TiO$_2$ synthesis suggests some potential for volumetric stabilization of the anatase polymorph through the prevention of the crystallite size reaching critical dimensions through particle growth or coarsening.

Scherrer analysis (Table S2) reveals that the minimum size of the anatase crystallites trends with diameter and, thus, the pore size of the SiO$_2$-NP templates (Table S1). Specifically, anatase crystallite sizes for 3DOm materials calcined at 450 °C range from 6.3 nm (T-450-s15-600) to 12.3 nm (T-773-s34-600) and fall below the critical nucleus size. Moreover, the SiO$_2$-NP template appears to prevent coarsening of the TiO$_2$ crystals upon calcination at 773 °C; this is noted by the lack of any significant increase in crystallite size in comparison to the 3DOm TiO$_2$ samples calcined at 450 °C. Conversely, significant anatase crystallite coarsening occurs in the absence of the template from ca. 12 nm anatase and rutile crystallites at 450 °C (T-u-450) to ca. 51.4 nm pure rutile crystallites at 773 °C (T-u-773). This unhindered coarsening of the untempated samples allows the grain size to surpass the critical diameter necessary for anatase stabilization and coincides with a complete transformation to the rutile polymorph.

Interfacial Contributions to the Stabilization of Metastable 3DOm Polymorphism. The apparent relation-ship between the surface area of the template and the resulting polymorph that is generated suggests that an interfacial mechanism may also contribute to the preservation of the metastable anatase phase at elevated temperatures. This concept is derived from our recent report of anatase stabilization along the interface of thin TiO$_2$ films deposited on oxide support layers (i.e., TiO$_2$/SiO$_2$).[57] Specifically, we have shown that the anatase polymorph can be stabilized by the TiO$_2$-SiO$_2$ interface at temperatures well in excess of the characteristic Hüttig temperature identified for bulk TiO$_2$. This results from the apparent interface-mediated mitigation of atomic surface mobility that typically favors the polymorphic transformation from anatase to rutile in bulk powders.

To further understand the relative contributions of template-imposed interfacial and volumetric stabilization constraints in the case of 3DOm TiO$_2$, we have prepared TiO$_2$ replicas on templates composed of much larger submicrometer (ca. 400 nm) SiO$_2$ particles. This order-of-magnitude increase in template particle size relative to the SiO$_2$-NPs described up to now (15−34 nm) lowers the template surface area and increases the template pore size, the latter by a factor of more than 4 over the critical TiO$_2$ crystallite size. Whereas anatase fractions (Figure 2, Table S2) in the 400 nm TiO$_2$ decrease to ca. 84 and 80% after calcination treatments at 450 and 773 °C, respectively, a clear resistance to the anatase-to-rutile interconversion seems to persist. Without volumetric confine-ment such as that imposed by smaller SiO$_2$-NP templates, however, the rutile crystallites grow to ca. 32 nm whereas anatase crystallites in the same sample are measured at approximately 24 nm, which still exceeds the theoretical critical crystallite dimensions.

Even in the case where a 50/50 physical mixture of TiO$_2$ and SiO$_2$ powders was prepared, in which no volumetric confine-ment and only limited interfacial interactions between phases were present, calcination to 773 °C resulted in limited but measurable resistance to the full anatase-to-rutile trans-formation. Specifically, a 14% anatase fraction was preserved (Table S2). These examples of persistent anatase stabilization without significant or specific volumetric confinement seem to point to an apparent role of the template−replica interface in stabilizing porous metastable TiO$_2$.

It is insightful to compare these findings to the templating of three-dimensionally ordered macroporous (3DOM) TiO$_2$ materials, reported previously by Holland and Stein,[20] realized

by the replication of ca. 400 nm polystyrene (latex) colloidal crystals. As we have described above to be the case with SiO_2 templates, Holland et al. demonstrated a similar resistance to bulklike TiO_2 polymorphism upon calcination employed for the removal of the organic template. Specifically, a purely anatase 3DOM structure was synthesized at a temperature of 575 °C, and the anatase polymorph persisted in fractional form with rutile at temperatures as high as 1000 °C. Such polymorphic stabilization under moderate confinement imposed by the 400 nm styrene templates in that work like that observed for SiO_2 templates here suggests that it may not be the specific surface composition so much as the interfacial confinement of crystallization that contributes to the observed stabilization phenomenon. This is consistent with our recent reports of two-dimensional interfacial confinement as a basis for the polymorphic stabilization of thin TiO_2 films.[57]

Fine Tuning TiO_2 Polymorphism via Surface Modification with SiO_2. Nonetheless, to further explore the template−replica interfacial influence on 3DOm TiO_2 materials and to determine whether the interface itself might be employed to fine tune the polymorphic phase stability, we have studied whether simple changes in the surface chemistry of the SiO_2-NP template may also influence fractional polymorphism. Specifically, we have tuned the template silanol chemistry by condensing surface hydroxyls into siloxane bonds (i.e., Si−O−Si)[58] through high-temperature calcination of the SiO_2-NP templates prior to 3DOm TiO_2 replication. The evolution in surface chemistry from as-made templates (treatment at 70 °C (I)) to those calcined at 600 °C (II)) is shown by FTIR characterization in Figure 3a. Whereas as-made templates (70 °C (I)) display a surface composition rich in
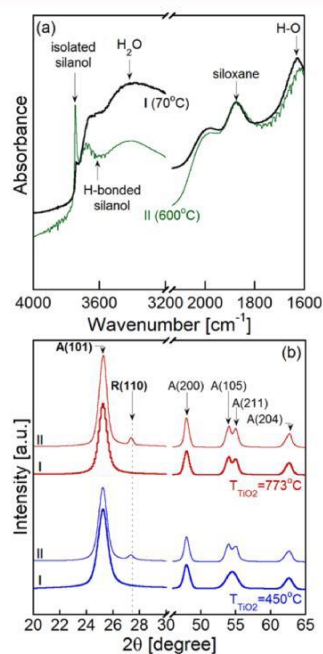
vicinal silanol groups (i.e., neighboring H-bonded Si−O−H, $v \approx 3530$ cm^{-1}), calcination at 600 °C (II) results in a weakening of the vicinal silanol band in favor of a more pronounced band at ~3741 cm^{-1} associated with isolated silanol groups.[59]

XRD data for 3DOm TiO_2 samples prepared on these disparately pretreated SiO_2-NP templates after composite TiO_2/SiO_2 calcination at 450 and 773 °C is also shown in Figure 3b. Template pretreatment at 70 °C (I) appears to generally prevent the development of the rutile polymorph (samples T-450-s34-70 and T-773-s34-70 in Table S2). Conversely, 600 °C pretreatment (II) of the SiO_2-NP template leads to the development of fractional rutile polymorphism upon composite TiO_2/SiO_2 calcination. XRD and TEM images collected at various stages of the IWI process (i.e., with iterative IWI infiltrations (between 1 and 7 times) of the SiO_2-NP template) (Figure 4), however, suggest that the onset of fractional rutile polymorphism in the case of templates pretreated at 600 °C does not occur until the later stages of
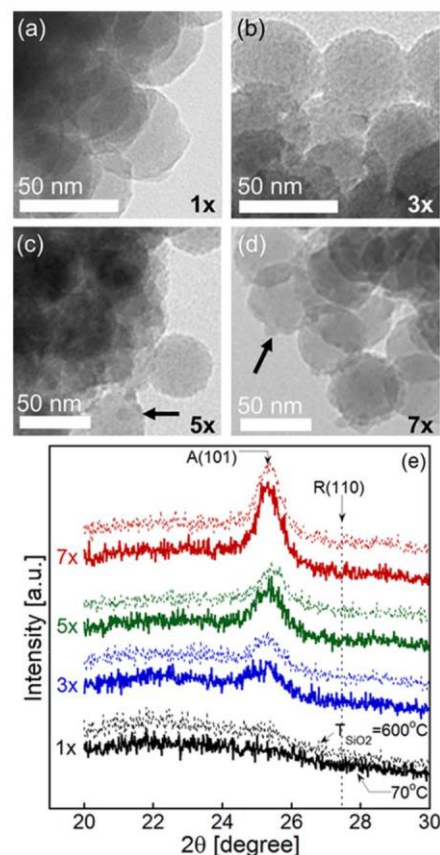

Figure 4. TEM micrographs showing the morphological evolution of TiO_2 when supported on ca. 50 nm SiO_2 nanoparticle crystal templates following sequential (a) 1×, (b) 3×, (c) 5×, and (d) 7× incipient wetness infiltrations (IWIs) of TiO_2 precursor materials and subsequent calcination at 773 °C for 3 h. Representative coarsening crystallites are shown by the arrows in panels (c) and (d). Corresponding XRD spectra of the SiO_2-NP-supported TiO_2 are shown in (e) for IWI of the TiO_2 precursor in SiO_2 templates that were either pretreated at $T_{SiO_2} = 70$ °C (solid lines) or precalcined at $T_{SiO_2} = 600$ °C (dashed lines). The position of the rutile R(110) reflection has been denoted to emphasize its absence in materials prepared with as many as 7× IWIs.

Figure 3. (a) FTIR characterization of the as-prepared, (I) (70 °C), and precalcined, (II) (600 °C), SiO_2 templates revealing correspond-ing changes in surface chemistry with calcination. (b) XRD (shifted for clarity) of 3DOm TiO_2 materials calcined in the presence of a 34 nm SiO_2-NP template for 3 h at 450 or 773 °C as specified for samples prepared by 9× incipient wetness infiltrations (IWIs) of 34 nm SiO_2-NP templates that have been either (I) pretreated at 70 °C or (II) precalcined at 600 °C prior to IWI.

the multiple infiltration process after a higher loading of surface-anchored TiO_2 crystallites is reached.

Specifically, TEM images show that after the 1× IWI step the SiO_2-NPs appear smooth with little evidence of TiO_2 decoration (Figure 4a). Subsequent IWI steps (i.e., 3−5× steps) generate small TiO_2 crystallites ∼5−10 nm in size anchored to the template surface (Figure 4b,c), and further IWI steps (i.e., 7×) result in larger surface-anchored TiO_2 crystallites that begin to fill the interstitial pore space of the SiO_2-NP template (Figure 4d). Corresponding XRD (Figure 4e) of the composite TiO_2/SiO_2 samples shows the persistence of purely the anatase polymorph, as denoted by the presence of the A(101) reflection and the absence of the R(110) peak during successive precursor loadings for SiO_2-NP templates pretreated at both (I) 70 °C (solid spectra) and (II) 600 °C (dashed spectra). This leaves the development of mixed anatase−rutile polymorphs, in the case of the SiO_2-NP templates pretreated at 600 °C (Figures 2 and 3), to the final stages of infiltration (i.e., after 9 successive IWI cycles).

Bright-field (BF) and high-angle annular dark-field (HAADF) STEM images of representative TiO_2 crystallites decorating the surface of the 600 °C-pretreated amorphous SiO_2-NP template after calcination at 773 °C are shown in Figures 5 and S5. Our analysis shows that samples are dominated by crystallites such as the one shown in Figure 5a for which the measured d spacing of lattice fringes corresponds to anatase {101} planes (3.52 Å) as opposed to rutile. Generally, the amorphous SiO_2 substrate is also observed to creep onto the surface of the TiO_2 crystallites (shown by the arrows in Figure 5a), providing increased interfacial contact
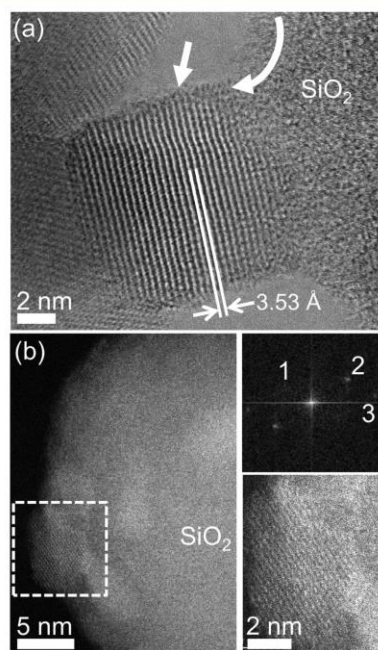

Figure 5. Representative BF- and HAADF-STEM images of TiO_2-decorated SiO_2-NP templates prepared via 7× IWI steps and calcination at 773 °C. The majority of TiO_2 crystallites have (a) lattice fringes that are consistent with anatase TiO_2 {101} (3.52 Å) and display wetting by a thin SiO_2 layer (arrowed) that appears to be fed from the substrate (denoted by the curved arrow). Panel (b) shows a minority SiO_2-supported crystallite (magnification shown in inset) bearing cross-fringes with the corresponding fast Fourier transform (FFT) indexed as rutile (Table S4).

between the TiO_2 and SiO_2 phases. Such surface migration of silica is expected given the sample calcination at 773 °C, which exceeds the characteristic Hüttig temperature of silica ($SiO_2^{Hüttig} \approx 570$ °C) where surface migration of atoms in bulk SiO_2 materials occurs.[60]

Although the overwhelming majority of the crystallites studied in detail by STEM imaging displayed lattice fringe spacings and angles that could be best indexed as anatase TiO_2 (Figure S5), one crystallite, shown in Figure 5b, was identified that was more consistent with the rutile polymorph of TiO_2. The fact that powder XRD (Figure 4) points to predominant anatase polymorphism for this sample is consistent with the minority rutile and massive majority of anatase crystallites (Figure S5) that were identified during our STEM analysis. It is also noteworthy that the rutile crystallite identified in Figure 5b does not show clear wetting by an amorphous SiO_2 film as observed in most cases for the anatase crystallites.

We hypothesize that the copious neighboring silanols, which decorate the surface of the as-made SiO_2 templates (Figure 3b(I)),[59] offer abundant sites for condensation with the alkoxide TiO_2 precursor during IWI and subsequent high-temperature processing.[24,25] Additionally, these sites most likely facilitate improved anchoring and dispersion of the TiO_2 precursor and provide more intimate interfacial contact between the TiO_2 crystallites and the underlying SiO_2 template relative to templates pretreated at 600 °C. Indeed, the wetting of isolated crystallites by SiO_2 thin films also appears to enhance the interfacial stabilization of anatase crystallites. Increased loading of TiO_2 crystallites closely adhered to the SiO_2 surface probably also leads to a degree of confinement-based stabilization as we have reported recently,[57] consistent with the apparent interface-mediated stabilization observed even for nonsiliceous templates (e.g., styrene[20]) as discussed earlier.

In the case of SiO_2-NP templates calcined at 600 °C, once the vicinal silanol groups are saturated by adhered crystallites, the higher proportion of isolated silanol groups (Figure 3b(II)) most likely leads to reduced adhesion and the onset of rutile polymorphism in the final stages of multicycle IWI-based synthesis. The differences in the nature of the SiO_2-NP substrate upon pretreatment seem to be manifested in limited SiO_2 wetting of these crystallites.

Generalizability of 3DOm MO_x Stabilization: Exten-sion to 3DOm ZrO_2 Templating. We have employed ZrO_2 as a surrogate metal oxide system in order to determine the applicability and generalizability of the 3DOm templating strategy and polymorphic stabilization phenomenon beyond TiO_2. Specifically, we synthesized 3DOm ZrO_2 using an iterative IWI procedure for the replication of a 34 nm SiO_2-NP template with a zirconyl chloride precursor, followed by calcination of the template−replica composite at 500 °C and template removal. TEM characterization of the product in Figure 6a shows ordered mesoporosity similar to that found for 34 nm 3DOm TiO_2, confirming the successful extension of the 3DOm templating approach to ZrO_2. The ordered meso-structure observed in the case of the templated material stands in stark contrast to the untemplated ZrO_2 control (Figure S4).

The characteristic hysteresis loop in the corresponding N_2 physisorption isotherm in Figure 6b demonstrates the retention of the mesoporosity upon template removal. As in the case of TiO_2, 3DOm templating of ZrO_2 results in narrowly distributed mesopores (inset, Figure 6) of ca. 17.3 nm as estimated by BJH analysis, a specific BET surface area (181 m²/g) that is more
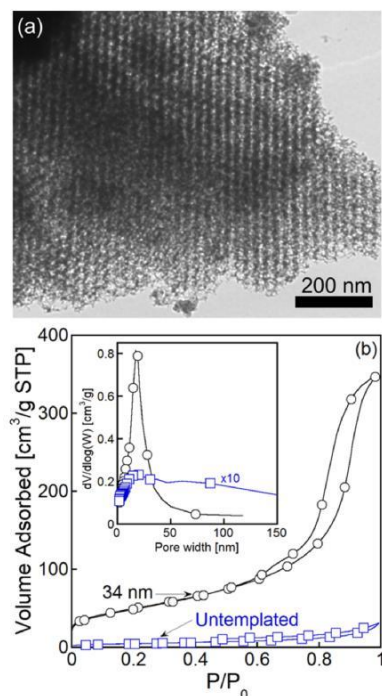
Figure 6. Analysis of the structure of 3DOm ZrO$_2$ templated upon a SiO$_2$-NP crystal composed of ca. 34 nm constituent particles after calcination to 500 °C and removal of the template. (a) Representative TEM micrograph and (b) nitrogen physisorption analysis (inset, pore size distribution by BJH) reveal the ordered mesostructuring and pore character relative to those of untemplated ZrO$_2$.
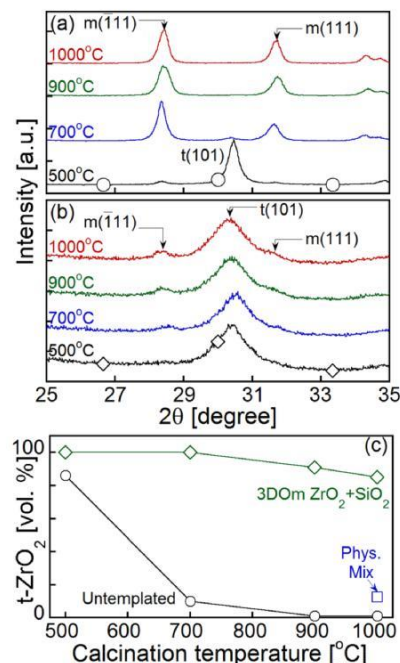

Figure 7. XRD data as a function of calcination temperature for (a) untemplated ZrO$_2$ and (b) a 3DOm ZrO$_2$/SiO$_2$ composite prepared by incipient wetness infiltration of a 34 nm SiO$_2$ colloidal crystal and calcination with the SiO$_2$ template in place. Panel (c) summarizes the corresponding relative tetragonal, t(101), polymorph content as a function of calcination temperature in comparison to a ZrO$_2$/SiO$_2$ physical mixture consisting of 53 wt % ZrO$_2$ physically ground with a 50 nm colloidal SiO$_2$ powder.

than an order of magnitude larger than that for the untemplated ZrO$_2$ control sample (i.e., 17 m^2/g, sample z-u-500), and a large specific pore volume of 0.5 cm^3/g as tabulated in Table S3.

Comparative XRD of untemplated (Figure 7a) and 3DOm ZrO$_2$ samples (Figure 7b) as a function of calcination conditions reveals an apparent stabilization of the correspond-ing metastable (tetragonal ZrO$_2$, t-ZrO$_2$) polymorph analogous to that which we observed for anatase TiO$_2$. Specifically, XRD data are shown for 34 nm 3DOm ZrO$_2$ (Figure 7b) following calcination of the SiO$_2$-ZrO$_2$ composite at temperatures ranging from 500 °C, where bulk ZrO$_2$ crystallization is expected, to temperatures below (700 °C), near (900 °C), and above (1000 °C), the characteristic Hüttig temperature for bulk ZrO$_2$ (ZrO$_2$$^{\text{Hüttig}} \approx$ 903 °C). The metastable tetragonal polymorph (as evidenced by the t(101) reflection at $2\theta \approx 30.2°$) persists under all conditions, with the development of no more than 15% thermodynamically stable m-ZrO$_2$ (Table S3, Figure 7c) indicated by a moderate increase in the characteristic m(111) ($2\theta \approx 31.5°$) and m($\bar{1}11$) ($2\theta \approx 28.2°$) reflections (Figure 7b). Under the same conditions, the untemplated ZrO$_2$ control sample fully converts to the thermodynamically stable monoclinic polymorph (Figure 7a,c, Table S3), as expected, once the characteristic Hüttig temperature has been reached.

As shown in Table S3, the 3DOm ZrO$_2$ crystallite size is limited to dimensions commensurate with the 34 nm SiO$_2$-NP template pore size (ca. 14 nm, Table S1), which is well below the critical nucleus size for t-ZrO$_2$ (~30 nm[61,62]). This points to the potential role of volumetric confinement in the observed polymorph stabilization. By final analogy with the 3DOm TiO$_2$ system, we show that a physical SiO$_2$−ZrO$_2$ mixture that provides no specific volumetric confinement of the ZrO$_2$ phase during coarsening and only moderate SiO$_2$−ZrO$_2$ interfacial

contact undergoes a transformation to ca. 88% m-ZrO$_2$ under composite calcination at 1000 °C (Figure 7c, Table S3). The limited but measurable resistance against full tetragonal-to-monoclinic transformation underscores the apparent contribu-tion, at least in part, of interfacial stabilization in the case of ZrO$_2$, as we have shown previously for TiO$_2$.

It is insightful to frame the 3DOm ZrO$_2$ results in the context of earlier literature reports of analogous macroporous 3DOM ZrO$_2$ materials templated upon poly(methyl meth-acrylate) (PMMA) colloidal crystals composed of ca. 300 nm particles. Namely, Al-Daous and Stein[63] showed that the PMMA template offered a degree of resistance to full polymorph interconversion, with as much as 54% t-ZrO$_2$ persisting at temperatures as high as 700 °C. As with TiO$_2$, the possible interfacial and confinement-mediated stabilization phenomena appear to be relatively independent of the specific template composition. This demonstrates the potential general-izability of the observed stabilization phenomenon among 3DOm MO$_x$ systems.

CONCLUSIONS

We have shown how a versatile colloidal crystal template composed of nanoparticles, ranging in diameter from 15 to 34 nm, can be employed to realize 3DOm TiO$_2$ and ZrO$_2$ replica structures with attractive surface areas, pore size tunability with near-nanometer resolution, and good control over polymorphic content. Specifically, this study elucidates the important role that the template plays in scaffolding the mesoporous product at temperatures that would traditionally collapse the pore structure of the oxide and goes on further to elucidate the role of the template in resisting the temperature-induced poly-

morphic transformation. Specifically, template-mediated interface and volumetric confinement effects combine to stabilize the metastable polymorphic phase of templated oxides during high-temperature calcination of the composite samples (i.e., TiO_2/SiO_2 and ZrO_2/SiO_2). The versatility of the geometrically simple SiO_2-NP templates for tailoring structure across meso- to microscopic scales makes the 3DOm templating approach a potentially attractive strategy for designing and tailoring material complexity.

■ ASSOCIATED CONTENT

*

TEM and N_2 physisorption characterization of SiO_2-NP templates; quantification of polymorphic and physical properties of 3DOm TiO_2, 3DOm ZrO_2, SiO_2-TiO_2, and SiO_2-ZrO_2 physical mixtures, and respective untemplated materials; and BF- and HAADF-STEM images of TiO_2 crystallites supported on SiO_2-NP templates with corresponding lattice fringe fitting (PDF)

■ AUTHOR INFORMATION

Corresponding Author

*E-mail: snyder@lehigh.edu. Phone: (610) 758-6834. Fax: (610) 758-5057.

ORCID ⊙

Li Lu: 0000-0002-6688-1176

Mark A. Snyder: 0000-0002-8925-0588

Author Contributions

§These authors contributed equally to this work.

Notes

The authors declare no competing financial interest.

■ REFERENCES

(1) Gu, D.; Schüth, F. Synthesis of Non-Siliceous Mesoporous Oxides. Chem. Soc. Rev. 2014, 43 (1), 313−344.

(2) Vlachos, D. G.; Chen, J. G.; Gorte, R. J.; Huber, G. W.; Tsapatsis, M. Catalysis Center for Energy Innovation for Biomass Processing: Research Strategies and Goals. Catal. Lett. 2010, 140 (3−4), 77−84.

(3) Basic Research Needs Catalysis for Energy; Washington, D.C., 2008.

(4) Fierro, J. L. G. Metal Oxides: Chemistry and Applications; CRC Press, 2005.

(5) Jacobsen, H.; Kleinschmit, P. Flame Hydrolysis. In Preparation of Solid Catalysts; Ertl, G., Knözinger, H., Eds.; Wiley-VCH: Weinheim, Germany, 1959; pp 99−109.

(6) White, L. J.; Duffy, G. J. Vapor-Phase Production of Colloidal Silica. Ind. Eng. Chem. 1959, 51 (3), 232−238.

(7) Boudart, M. Irreducible Transport Phenomena in Chemical Kinetics. Kinetics of Chemical Processes; Prentice-Hall: Englewood Cliffs, NJ, 1968; pp 144−164.

(8) Boudart, M.; Djega-Mariadassou, G. Parasitic Phenomena. Kinetics of Heterogeneous Catalytic Reactions; Princeton University Press: Princeton, NJ, 1984; pp 194−201.

(9) Froment, G. F.; Bischoff, K. B.; De Wilde, J. Fixed Bed Catalytic Reactors. Chemical Reactor Analysis and Design; John Wiley & Sons: Hoboken, NJ, 2010; pp 548−558.

(10) Stevenson, S. A.; Ruckenstein, E. Mechanisms of Sintering (Migration and Coalescence). In Metal-Support Interactions in Catalysis, Sintering, and Redispersion; Van Nostrand Reinhold: New York, 1987; pp 156−186.

(11) Rouquerol, J.; Avnir, D.; Fairbridge, C. W.; Everett, D. H.; Haynes, J. H.; Pernicone, N.; Ramsay, J. D. F.; Sing, K. S. W.; Unger, K. K. Recommendations for the Characterization of Porous Solids. Pure Appl. Chem. 1994, 66 (8), 1739−1758.

(12) Holland, B. T.; Blanford, C. F.; Stein, A. Synthesis of Macroporous Minerals with Highly Ordered Three-Dimensional Arrays of Spheroidal Voids. Science 1998, 281 (5376), 538−540.

(13) McLachlan, M. A.; Barron, C. C. A.; Johnson, N. P.; De La Rue, R. M.; McComb, D. W. Preparation of Large Area Three-Dimensionally Ordered Macroporous Thin Films by Confined Infiltration and Crystallisation. J. Cryst. Growth 2008, 310 (10), 2644−2648.

(14) Kuai, S.-L.; Truong, V.-V.; Hache, A.; Hu, X.-F. A Comparative Study of Inverted-Opal Titania Photonic Crystals Made from Polymer and Silica Colloidal Crystal Templates. J. Appl. Phys. 2004, 96 (11), 5982−5986.

(15) Snyder, M. A. Deriving Hierarchical Complexity from Simplistic Colloidal Templates. MRS Bull. 2016, 41 (9), 683−688.

(16) Stein, A.; Li, F.; Denny, N. R. Morphological Control in Colloidal Crystal Templating of Inverse Opals, Hierarchical Structures, and Shaped Particles. Chem. Mater. 2008, 20 (3), 649−666.

(17) Ding, H.; Sun, H.; Shan, Y. Preparation and Characterization of Mesoporous SBA-15 Supported Dye-Sensitized TiO_2 Photocatalyst. J. Photochem. Photobiol., A 2005, 169 (1), 101−107.

(18) Zhang, Z.; Zuo, F.; Feng, P. Hard Template Synthesis of Crystalline Mesoporous Anatase TiO_2 for Photocatalytic Hydrogen Evolution. J. Mater. Chem. 2010, 20, 2206−2212.

(19) Zhou, W.; Sun, F.; Pan, K.; Tian, G.; Jiang, B.; Ren, Z.; Tian, C.; Fu, H. Well-Ordered Large-Pore Mesoporous Anatase TiO_2 with Remarkably High Thermal Stability and Improved Crystallinity: Preparation, Characterization, and Photocatalytic Performance. Adv. Funct. Mater. 2011, 21 (10), 1922−1930.

(20) Holland, B. T.; Blanford, C. F.; Do, T.; Stein, A. Synthesis of Highly Ordered, Three-Dimensional Macroporous Structures of Amorphous or Crystalline Inorganic Oxides, Phophates, and Hybrid Composites. Chem. Mater. 1999, 11 (3), 795−805.

(21) Fan, W.; Snyder, M. A.; Kumar, S.; Lee, P.-S.; Yoo, W. C.; McCormick, A. V.; Penn, R. L.; Stein, A.; Tsapatsis, M. Hierarchical Nanofabrication of Microporous Crystals with Ordered Mesoporosity. Nat. Mater. 2008, 7 (12), 984−991.

(22) Stein, A. Sphere Templating Methods for Periodic Porous Solids. Microporous Mesoporous Mater. 2001, 44−45, 227−239.

(23) Velev, O. D.; Lenhoff, A. M. Colloidal Crystals as Templates for Porous Materials. Curr. Opin. Colloid Interface Sci. 2000, 5 (1−2), 56− 63.

(24) Livage, J.; Henry, M.; Sanchez, C. Sol-Gel Chemistry of Transition Metal Oxides. Prog. Solid State Chem. 1988, 18 (4), 259− 341.

(25) Turova, N. Y.; Turevskaya, E. P.; Kessler, V. G.; Yanovskaya, M. I. Hydrolysis of Metal Alkoxides and Synthesis of Simple Oxides by the Sol-Gel Method. The Chemistry of Metal Alkoxides; Springer, 2002; pp 107−125.

(26) Sun, X.; Shi, Y.; Zhang, P.; Zheng, C.; Zheng, X.; Zhang, F.; Zhang, Y.; Guan, N.; Zhao, D.; Stucky, G. D. Container Effect in Nanocasting Synthesis of Mesoporous Metal Oxides. J. Am. Chem. Soc. 2011, 133 (37), 14542−14545.

(27) Crossland, E. J. W.; Noel, N.; Sivaram, V.; Leijtens, T.; Alexander-Webber, J. A.; Snaith, H. J. Mesoporous TiO_2 Single

Crystals Delivering Enhanced Mobility and Optoelectronic Device Performance. Nature 2013, 495 (7440), 215−220.

(28) Bian, Z.; Zhu, J.; Wen, J.; Cao, F.; Huo, Y.; Qian, X.; Cao, Y.; Shen, M.; Li, H.; Lu, Y. Single-Crystal-like Titania Mesocages. Angew. Chem., Int. Ed. 2011, 50 (5), 1105−1108.

(29) Kim, S. S.; Lee, H. I.; Shon, J. K.; Hur, J. Y.; Kang, M. S.; Park, S. S.; Kong, S. S.; Yu, J. A.; Seo, M.; Li, D.; et al. Preparation of Highly Ordered Mesoporous TiO2 Materials with Crystalline Framework from Different Mesostructured Silica Templates via Nanoreplication. Chem. Lett. 2008, 37 (2), 140−141.

(30) Yonemoto, B. T.; Guo, Q.; Hutchings, G. S.; Yoo, W. C.; Snyder, M. A.; Jiao, F. Observation of Strain in Ordered Mesoporous TiO2 Anatase as Lithium Intercalation Electrode. Chem. Commun. (Cambridge, U. K.) 2014, 50, 8997−8999.

(31) Snyder, M. A.; Lee, J. A.; Davis, T. M.; Scriven, L. E.; Tsapatsis, M. Silica Nanoparticle Crystals and Ordered Coatings Using Lys-Sil and a Novel Coating Device. Langmuir 2007, 23 (20), 9924−9928.

(32) Davis, T. M.; Snyder, M. A.; Krohn, J. E.; Tsapatsis, M. Nanoparticles in Lysine-Silica Sols. Chem. Mater. 2006, 18 (25), 5814−5816.

(33) Yokoi, T.; Sakamoto, Y.; Terasaki, O.; Kubota, Y.; Okubo, T.; Tatsumi, T. Periodic Arrangement of Silica Nanospheres Assisted by Amino Acids. J. Am. Chem. Soc. 2006, 128 (42), 13664−13665.

(34) Vogel, N.; Retsch, M.; Fustin, C.-A.; del Campo, A.; Jonas, U. Advances in Colloidal Assembly: The Design of Structure and Hierarchy in Two and Three Dimensions. Chem. Rev. 2015, 115, 6265−6311.

(35) Kung, S. C.; Chang, C.-C.; Fan, W.; Snyder, M. A. Template-Free Ordered Mesoporous Silicas by Binary Nanoparticle Assembly. Langmuir 2014, 30 (39), 11802−11811.

(36) Kuroda, Y.; Sakamoto, Y.; Kuroda, K. Selective Cleavage of Periodic Mesoscale Structures: Two-Dimensional Replication of Binary Colloidal Crystals into Dimpled Gold Nanoplates. J. Am. Chem. Soc. 2012, 134 (20), 8684−8692.

(37) Bickley, R. I.; Gonzalez-Carreno, T.; Lees, J. S.; Palmisano, L.; Tilley, R. J. D. A Structural Investigation of Titanium Dioxide Photocatalysts. J. Solid State Chem. 1991, 92 (1), 178−190.

(38) Zhang, Q.; Gao, L.; Guo, J. Effects of Calcination on the Photocatalytic Properties of Nanosized TiO2 Powders Prepared by TiCl4 Hydrolysis. Appl. Catal., B 2000, 26 (3), 207−215.

(39) Ohno, T.; Sarukawa, K.; Tokieda, K.; Matsumura, M. Morphology of a TiO2 Photocatalyst (Degussa, P-25) Consisting of Anatase and Rutile Crystalline Phases. J. Catal. 2001, 203 (1), 82−86.

(40) Yan, M.; Chen, F.; Zhang, J.; Anpo, M. Preparation of Controllable Crystalline Titania and Study on the Photocatalytic Properties. J. Phys. Chem. B 2005, 109 (18), 8673−8678.

(41) Cong, S.; Xu, Y. Explaining the High Photocatalytic Activity of a Mixed Phase TiO2: A Combined Effect of O2 and Crystallinity. J. Phys. Chem. C 2011, 115, 21161−21168.

(42) Zhang, Y.; Deng, L.; Zhang, G.; Gan, H. Facile Synthesis and Photocatalytic Property of Bicrystalline TiO2/Rectorite Composites. Colloids Surf., A 2011, 384 (1−3), 137−144.

(43) O'Regan, B.; Gratzel, M. A Low-Cost, High-Efficiency Solar-Cell Based on Dye-Sensitized Colloidal TiO2 Films. Nature 1991, 353 (6346), 737−740.

(44) Soultanidis, N.; Zhou, W.; Psarras, A. C.; Gonzalez, A. J.; Iliopoulou, E. F.; Kiely, C. J.; Wachs, I. E.; Wong, M. S. Relating N-Pentane Isomerization Activity to the Tungsten Surface Density of WOₓ/ZrO2. J. Am. Chem. Soc. 2010, 132 (38), 13462−13471.

(45) Ross-Medgaarden, E. I.; Knowles, W. V.; Kim, T.; Wong, M. S.; Zhou, W.; Kiely, C. J.; Wachs, I. E. New Insights into the Nature of the Acidic Catalytic Active Sites Present in ZrO2-Supported Tungsten Oxide Catalysts. J. Catal. 2008, 256 (1), 108−125.

(46) Hartlen, K. D.; Athanasopoulos, A. P. T.; Kitaev, V. Facile Preparation of Highly Monodisperse Small Silica Spheres (15 to 200 Nm) Suitable for Colloidal Templating and Formation of Ordered Arrays. Langmuir 2008, 24 (5), 1714−1720.

(47) Yokoi, T.; Wakabayashi, J.; Otsuka, Y.; Fan, W.; Iwama, M.; Watanabe, R.; Aramaki, K.; Shimojima, A.; Tatsumi, T.; Okubo, T.

Mechanism of Formation of Uniform-Sized Silica Nanospheres Catalyzed by Basic Amino Acids. Chem. Mater. 2009, 21 (15), 3719−3729.

(48) Brunauer, S.; Emmett, P. H.; Teller, E. Adsorption of Gases in Multimolecular Layers. J. Am. Chem. Soc. 1938, 60 (1), 309−319.

(49) Barrett, E. P.; Joyner, L. G.; Halenda, P. P. The Determination of Pore Volume and Area Distributions in Porous Substances. I. Computations from Nitrogen Isotherms. J. Am. Chem. Soc. 1951, 73 (1), 373−380.

(50) Toraya, H.; Yoshimura, M.; Somiya, S. Calibration Curve for Quantitative Analysis of the Monoclinic-Tetragonal ZrO2 System by X-Ray Diffraction. J. Am. Ceram. Soc. 1984, 67 (6), C119−C121.

(51) Spurr, R. A.; Myers, H. Quantitative Analysis of Anatase-Rutile Mixtures with an X-Ray Diffractometer. Anal. Chem. 1957, 29 (5), 760−762.

(52) Cullity, B. D. Diffraction I: The Direction of Diffracted Beams. Elements of X-ray Diffraction; Addison-Wesley: Reading, MA, 1956; pp 96−102.

(53) Thommes, M.; Kaneko, K.; Neimark, A. V.; Olivier, J. P.; Rodriguez-Reinoso, F.; Rouquerol, J.; Sing, K. S. W. Physisorption of Gases, with Special Reference to the Evaluation of Surface Area and Pore Size Distribution. Pure Appl. Chem. 2015, 87 (9−10), 1051− 1069.

(54) Hanaor, D. A. H.; Sorrell, C. C. Review of the Anatase to Rutile Phase Transformation. J. Mater. Sci. 2011, 46 (4), 855−874.

(55) Ranade, M. R.; Navrotsky, A.; Zhang, H. Z.; Banfield, J. F.; Elder, S. H.; Zaban, A.; Borse, P. H.; Kulkarni, S. K.; Doran, G. S.; Whitfield, H. J. Energetics of Nanocrystalline TiO2. Proc. Natl. Acad. Sci. U. S. A. 2002, 99, 6476−6481.

(56) Zhang, H.; Banfield, J. F. Understanding Polymorphic Phase Transformation Behavior during Growth of Nanocrystalline Aggre-gates: Insights from TiO2. J. Phys. Chem. B 2000, 104 (15), 3481− 3487.

(57) Gregory, D. G.; Lu, L.; Kiely, C. J.; Snyder, M. A. Interfacial Stabilization of Metastable TiO2 Films. J. Phys. Chem. C 2017, 121, 4434−4442.

(58) Comas-Vives, A. Amorphous SiO2 Surface Models: Energetics of the Dehydroxylation Process, Strain, Ab Initio Atomistic Thermodynamics and IR Spectroscopic Signatures. Phys. Chem. Chem. Phys. 2016, 18 (10), 7475−7482.

(59) Iler, R. K. The Chemistry of Silica; John Wiley & Sons: New York, 1979.

(60) Ertl, G.; Knozinger, H.; Weitkamp, J. Spreading and Wetting. Preparation of Solid Catalysts; Wiley-VCH: Weinheim, Germany, 1999; pp 501−526.

(61) Garvie, R. C. The Occurrence of Metastable Tetragonal Zirconia as a Crystallite Size Effect. J. Phys. Chem. 1965, 69 (4), 1238−1243.

(62) Garvie, R. C. Stabilization of the Tetragonal Structure in Zirconia Microcrystals. J. Phys. Chem. 1978, 82 (2), 218−224.

(63) Al-Daous, M. A.; Stein, A. Preparation and Catalytic Evaluation of Macroporous Crystalline Sulfated Zirconium Dioxide Templated with Colloidal Crystals. Chem. Mater. 2003, 15 (13), 2638−2645.